Available online at www.sciencedirect.com
ScienceDirect
Journal of Sound and Vibration 320 (2009) 955–976
JOURNAL OF SOUND AND VIBRATION
www.elsevier.com/locate/jsvi

Decay rates of propagating waves in railway tracks at high frequencies

J. Ryue[a,*], D.J. Thompson[a], P.R. White[a], D.R. Thompson[b]

[a]*Institute of Sound and Vibration Research, University of Southampton, Highfield, Southampton SO17 1BJ, UK*
[b]*Balfour Beatty Rail Technologies, Midland House, Nelson Street, Derby DE1 2SA, UK*

Received 24 January 2008; received in revised form 1 September 2008; accepted 7 September 2008
Handling Editor: A.V. Metrikine
Available online 31 October 2008

Abstract

In order to understand long range wave propagation in railway tracks, it is required to identify how far vibrations can travel along a rail. To answer this question, the attenuation characteristics of the main propagating waves are required as a function of distance. In this work, decay rates of propagating waves in railway tracks are investigated for frequencies up to 80 kHz. A numerical method called the wavenumber finite element (WFE) method is utilized to predict decay rates for a rail on a continuous foundation. Damping is introduced in this track model by the material damping in the rail and in the foundation. In order to improve the simulated results, the frequency dependent damping loss factor of a rail has been measured up to 80 kHz on short rail samples. From this simulation, the relative importance of the rail and support damping for the long range wave propagation is determined. In order to validate the simulated results, a field measurement has been performed on an operational railway track. From this experiment, train-induced rail vibrations have been acquired for several running trains travelling over a long section of rail. The measured results are presented for comparison with the output of the simulations and good agreement is found between them.

1. Introduction

At high frequencies, waves in railway tracks are known to propagate over large distances. The purpose of the work described here is to determine how far waves can travel along a rail and to identify the waves that have the minimum decay rates. In particular, it is of interest to find the frequency range in which the maximum propagation occurs and the area of the rail on which this could be measured. In terms of the long range wave propagation along a railway track, it was suggested in Refs. [1,2] that frequencies up to 80 kHz need to be considered. Above 80 kHz it is known that the decay rates of waves in the rail increase. For frequencies up to 80 kHz, the effective wave types measurable on the rail surface were investigated in Ref. [3]. From the numerical simulations and test track measurements performed in Ref. [3], it was found that these effective

*Corresponding author. Tel.: +44 2380 593759; fax: +44 2380 593190.
E-mail address: J.Ryue@soton.ac.uk (J. Ryue).

0022-460X/$ - see front matter © 2008 Elsevier Ltd. All rights reserved.
doi:10.1016/j.jsv.2008.09.025

waves are a vertical bending wave that is localized in the rail head above 15 kHz, a lateral bending wave that mainly deforms the rail head and web above 20 kHz, and the first-order web bending wave above 10 kHz.

Now in order to justify whether these waves are capable of long range propagation, it has to be identified *how far along a rail these waves can travel*. To answer this question, the attenuation characteristics of propagating waves are required as a function of frequency up to 80 kHz. These results will also specify which frequency range is the most effective for long range wave propagation in railway tracks. Due to the presence of the multiple wave types and their complex dispersive behaviour, previous studies on identifying decay rates of waves propagating along railway tracks are limited, particularly at high frequencies.

For the purpose of wheel–rail rolling noise, Vincent et al. [4] measured the decay rates of several operational tracks over the range 100–5000 Hz by means of impact excitation. It was found, from comparison with the simulated results presented in Ref. [5], that a track model with a continuous support gives a good agreement with measured results at higher frequency. This is because the periodicity effect of a discrete support does not strongly influence high frequency waves. In addition, Thompson [6] developed an experimental analysis technique and obtained decay rates of propagating waves up to 6 kHz, using measured data taken on the track. However, these methods are not applicable for high frequencies up to 80 kHz because they would require a large number of measurement points along the rail and around its perimeter.

As an experimental method for the high frequency region, Lanza di Scalea et al. [7,8] applied an impulse excitation to the rail and measured the direct signals and echo signals reflected from the opposite end of a rail section. Comparing the direct and reflected signals, they extracted the frequency-dependent attenuation up to 50 kHz for a free rail. However, the possibility of the energy loss or mode conversion resulting from the reflecting end of the rail was not considered in this experiment. In addition, Rose et al. [1] measured waveforms at the top of the rail head at various distances along a free rail by using 60 kHz SH EMAT transducers. From this measurement they found a decay rate of about 0.56 dB/m at around 60 kHz. Detailed information on the wave types measured and the contribution of the rail foundation to decay rates in the high frequency region is lacking from both previous studies.

In terms of the numerical approach to track modelling, the wavenumber finite element (WFE) method has been used, particularly for high frequency analysis [2,9–11]. However, most of the previous work was confined to analyzing dispersion relations and group velocities in undamped free rails. Most recently, Bartoli et al. [12] presented decay rates of each wave propagating along a damped free rail by accounting for material damping up to 50 kHz. In this prediction, they introduced an energy velocity to obtain decay rates for damped media. As will be seen in the present work, although the minimum decay rates are mainly determined by the damping of the rail, if the effect of the support is omitted it is not possible to distinguish which waves have the lowest decay rates.

In the present study, the WFE method is applied to predict decay rates for a damped rail with a continuous damped foundation. In this prediction, decay rates are evaluated from damped wavenumbers of individual waves using a method derived by Nilsson [13]. Also, in order to improve the simulation results, damping loss factors are measured up to 80 kHz from impact hammer tests on three different rail samples. Then the decay rates are recalculated by using the measured damping loss factor for the rail. Finally, a field measurement was carried out on an operational railway track to validate the simulated decay rates over a longer section of rail. In this experiment train-induced rail vibrations from six in-service trains are measured at three different positions on the rail cross-section. The measured decay rates are compared with the simulated ones produced by WFE analysis.

2. Track model

In this study, a standard UIC60 rail section is modelled. Since the UIC60 rail has a symmetric cross-section, only half of the width is included, as shown in Fig. 1. This has an additional advantage of separating the possible waves into two groups that are uncoupled from each other. Thus, a symmetric boundary condition that constrains the deformation of the mid-plane in the lateral (y) direction gives the vertical and symmetric longitudinal modes; an antisymmetric boundary condition that constrains the remaining (x and z) directions in the mid-plane gives the lateral and torsional modes. In addition, the latter condition gives antisymmetric longitudinal modes in which opposite sides of the rail move in opposite directions. The rail clip is generally much more flexible than the rail pad [14] and is omitted from the model. In addition, since the contribution of

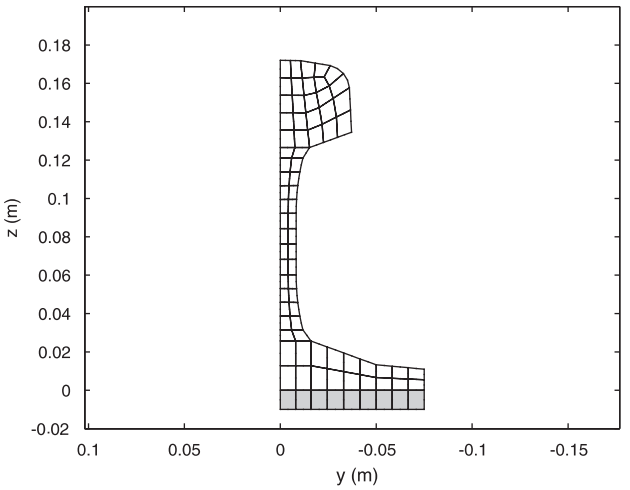

Fig. 1. The cross-sectional model of a rail on foundation for WFE analysis. The shaded elements represent the rail pad.

the sleeper and ballast is limited to the low frequency region, typically below 1 kHz [14], only the rail pad is included in this model. The track model shown in Fig. 1 is the same as used in Ref. [3] to determine the propagating wave types in a railway track at high frequencies.

In this track model, the rail pads are considered as a continuous elastic foundation. This appears to be a good approximation of the real situation at high frequencies as explained in Ref. [3]. The nominal stiffnesses of the single rail pad were chosen to be 150 MN/m in the vertical direction and 20 MN/m in the lateral and longitudinal directions. These values are typical of a modern resilient pad [4,6]. At high frequencies, however, the stiffness of the rail pad usually becomes much higher than the static or low frequency stiffness. This is because of internal resonances at high frequencies. This stiffening of the rail pad due to internal resonances is approximated by introducing dynamic stiffnesses which are 10 times larger than the nominal ones that were stated above [3]. As shown in Ref. [3], this tends to over-estimate the effect of the support below 20 kHz and under-estimate it above 20 kHz.

The cross-sectional FE model shown in Fig. 1 consists of quadrilateral solid elements which possess eight nodes each having three translational degrees of freedom. From the WFE analysis using this model, it was found that the deformation shape of the cross-section is well described with more than four elements (eight nodes) per wavelength for frequencies up to 80 kHz.

3. Prediction of decay rates using the WFE method

3.1. Predicted dispersion curves

For the track model in Fig. 1, the dispersion relations predicted by WFE analysis are shown in Fig. 2. Fig. 2(a) illustrates the vertical and symmetric longitudinal waves; Fig. 2(b) is for the lateral, torsional and antisymmetric longitudinal waves. The different waves in each graph are distinguished using various line styles and markers. From Fig. 2 it is found that there are 63 wave types in total in the rail in the frequency range up to 80 kHz. More detail of the dispersion relations and group velocities are presented in Ref. [3].

3.2. Formulation for decay rates

In WFE analysis, the partial differential equation of a structure which is infinitely long in one direction, here denoted the x-direction, and has a uniform cross-section along x, is given by

$$\left\{\mathbf{K}_2\frac{\partial^2}{\partial x^2}+\mathbf{K}_1\frac{\partial}{\partial x}+\mathbf{K}_0-\mathbf{M}\frac{\partial^2}{\partial t^2}\right\}\mathbf{W}(x,t)=\mathbf{0}, \tag{1}$$

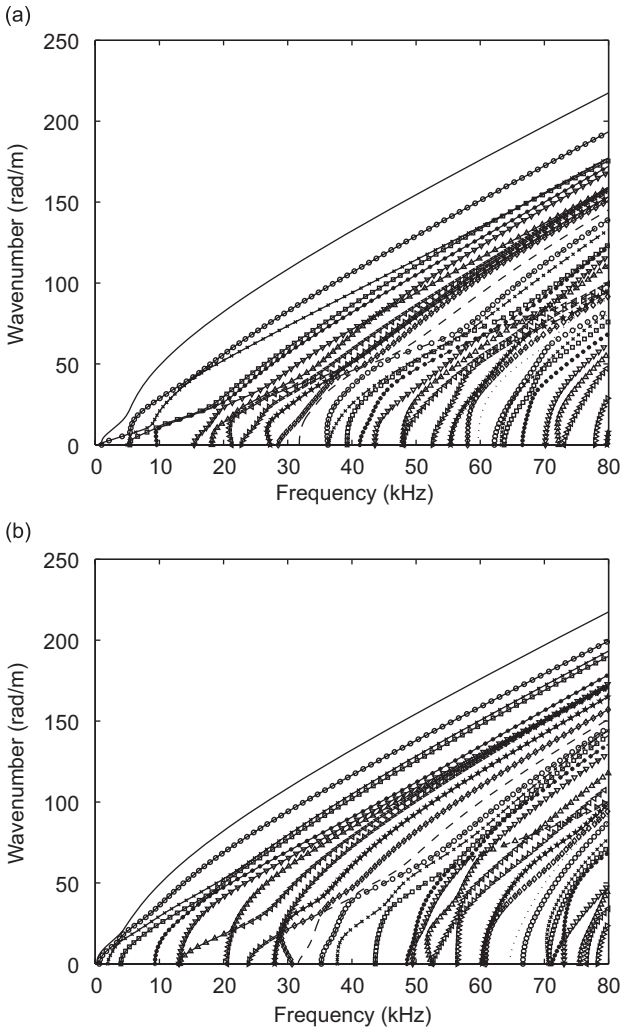

Fig. 2. Predicted dispersion curves of supported rail for (a) the vertical and symmetric longitudinal waves, (b) the lateral, torsional and antisymmetric longitudinal waves. Each wave is distinguished with various line styles and markers.

where $\mathbf{K}_2$, $\mathbf{K}_1$ and $\mathbf{K}_0$ are stiffness matrices, $\mathbf{M}$ is the mass matrix of the cross-section and $\mathbf{W}(x,t)$ is the displacement vector [13]. Since a harmonic wave solution will be introduced for the x direction in this method, all the matrices are independent of x and are real if there is no damping included. The displacement vector is defined as $\mathbf{W}(x,t)=\tilde{\mathbf{W}}e^{j(\omega t-\kappa x)}$, and then Eq. (1) becomes

$$\{\mathbf{K}-\omega^2\mathbf{M}\}\tilde{\mathbf{W}}=\mathbf{0}, \tag{2}$$

where $\mathbf{K}=\mathbf{K}_2(-j\kappa)^2+\mathbf{K}_1(-j\kappa)+\mathbf{K}_0$ and $\tilde{\mathbf{W}}$ indicates the displacements of the nodes on the cross-section defining deformation shapes of the waves. In this governing equation, κ and ω are the unknown variables to be identified. Eq. (2) can be solved as a generalized eigenvalue problem for the frequency ω if the wavenumber, κ, is given. Also, the group velocity, c_g, can readily be evaluated for each wave using this method, since

$$c_g=\frac{\partial\omega}{\partial\kappa}=\frac{\tilde{\mathbf{W}}^{\mathrm{H}}\mathbf{K}'\tilde{\mathbf{W}}}{2\omega\tilde{\mathbf{W}}^{\mathrm{H}}\mathbf{M}\tilde{\mathbf{W}}}, \tag{3}$$

where $\mathbf{K}'=\partial\mathbf{K}/\partial\kappa=-2\kappa\mathbf{K}_2-j\mathbf{K}_1$ and $\tilde{\mathbf{W}}^{\mathrm{H}}$ indicates a complex conjugate transpose of $\tilde{\mathbf{W}}$ [16].

So far all the WFE equations were derived for an undamped structure. Now suppose that damping is included in the model by adding an imaginary part to the real valued stiffness matrices as

$$\mathbf{K}_d = \mathbf{K}_2(1+\mathrm{j}\eta)(-\mathrm{j}\kappa)^2 + \mathbf{K}_1(1+\mathrm{j}\eta)(-\mathrm{j}\kappa) + \mathbf{K}_0(1+\mathrm{j}\eta) = \mathbf{K}(1+\mathrm{j}\eta), \tag{4}$$

where $\mathbf{K}_d$ indicates the complex stiffness matrix and η is the damping loss factor. For small damping, a damped wavenumber can be expressed approximately by a Taylor series as

$$\kappa_d \approx \kappa + \left.\frac{\partial \kappa_d}{\partial \eta}\right|_{\eta=0} \eta, \tag{5}$$

where κ and κ_d denote undamped and damped wavenumbers, respectively [13]. For a given frequency, the derivative with respect to η, in Eq. (5), can be evaluated as follows. Since the equation of motion has to be satisfied even if damping is slightly increased,

$$\frac{\partial}{\partial \eta}\{[\mathbf{K}_d - \omega^2\mathbf{M}]\tilde{\mathbf{W}}\} = \frac{\partial}{\partial \eta}\{[\mathbf{K}(1+\mathrm{j}\eta) - \omega^2\mathbf{M}]\tilde{\mathbf{W}}\} = \mathbf{0}. \tag{6}$$

As the stiffness matrix $\mathbf{K}_d$ is a function of κ_d, the derivative of this equation can be written as

$$\left[\mathrm{j}\mathbf{K} + \frac{\partial \mathbf{K}_d}{\partial \kappa_d}\frac{\partial \kappa_d}{\partial \eta}\right]\tilde{\mathbf{W}} + [\mathbf{K}_d - \omega^2\mathbf{M}]\frac{\partial}{\partial \eta}\tilde{\mathbf{W}} = \mathbf{0}. \tag{7}$$

By multiplying the above equation by the left eigenvector, $\tilde{\mathbf{W}}^L$, and then using the definition, $\tilde{\mathbf{W}}^{L^{\mathrm{T}}}[\mathbf{K} - \omega^2\mathbf{M}] = \mathbf{0}$, the resulting expression at $\eta = 0$ is given as

$$\left.\frac{\partial \kappa_d}{\partial \eta}\right|_{\eta=0} = \frac{-\mathrm{j}\tilde{\mathbf{W}}^{\mathrm{H}}\mathbf{K}\tilde{\mathbf{W}}}{\tilde{\mathbf{W}}^{\mathrm{H}}\mathbf{K}'\tilde{\mathbf{W}}}. \tag{8}$$

Since $\mathbf{K} = \omega^2\mathbf{M}$ when $\eta = 0$, this leads to

$$\left.\frac{\partial \kappa_d}{\partial \eta}\right|_{\eta=0} = \frac{-\mathrm{j}\omega^2\tilde{\mathbf{W}}^{\mathrm{H}}\mathbf{M}\tilde{\mathbf{W}}}{\tilde{\mathbf{W}}^{\mathrm{H}}\mathbf{K}'\tilde{\mathbf{W}}}. \tag{9}$$

Using the group velocity in Eq. (3), it follows that

$$\left.\frac{\partial \kappa_d}{\partial \eta}\right|_{\eta=0} = \frac{-\mathrm{j}\omega}{2c_g}. \tag{10}$$

Therefore, the damped wavenumber can be expressed as

$$\kappa_d = \kappa + \left.\frac{\partial \kappa_d}{\partial \eta}\right|_{\eta=0} \eta = \kappa - \frac{\mathrm{j}\omega}{2c_g}\eta. \tag{11}$$

Hence the decay rate, Δ in dB/m, can be obtained from the imaginary part of the damped wavenumber using

$$\Delta = -8.686\,\mathrm{Im}(\kappa_d) = 8.686\left(\frac{\omega\eta}{2c_g}\right) = 27.29\frac{f\eta}{c_g}. \tag{12}$$

3.3. Decay rates for a track model

In terms of energy loss from the rails, two different mechanisms could be considered: internal dissipation due to material damping of the rail and acoustic emission from the rail surface. However, the latter effect is predicted to be much smaller than the former one for most of the frequency range of interest. Hence, only the internal dissipation by the material damping is considered here. The predicted damping loss factor caused by acoustic emission will be compared with the measured damping loss factors of rails in Section 3.4.

Table 1
The elastic moduli of the rail and foundation for the stiffness matrices of $\mathbf{K}_r$ and $\mathbf{K}_p$

Elastic modulus	$\mathbf{K}_r$	$\mathbf{K}_p$
Young's modulus of rail (E_r) (GPa)	200	0
Young's modulus of foundation (E_p) (MPa)	0	166.7
Shear modulus of foundation (G_p) (MPa)	0	22.7

There are two damping components in the track model shown in Fig. 1: the damping in the rail, η_r, and that in the foundation, η_p. The stiffness matrix of this track model can be separated into two parts

$$\mathbf{K}_d = (1+\mathrm{j}\eta_r)\mathbf{K}_r + (1+\mathrm{j}\eta_p)\mathbf{K}_p, \tag{13}$$

where $\mathbf{K}_r$ and $\mathbf{K}_p$ denote the stiffness matrices for the rail and foundation, respectively. These stiffness matrices possess separate material properties for the rail and foundation as specified in Table 1. Because of the different dampings in the rail and foundation, the damped wavenumber of this track model has to be slightly modified from Eq. (11).

For this model a damped wavenumber, κ_d, can be expressed as

$$\kappa_d = \kappa + \left.\frac{\partial\kappa_d}{\partial\eta_r}\right|_{\eta_r=0}\eta_r + \left.\frac{\partial\kappa_d}{\partial\eta_p}\right|_{\eta_p=0}\eta_p. \tag{14}$$

By following the same process as described above, the two derivative terms in Eq. (14) become

$$\left.\frac{\partial\kappa_d}{\partial\eta_r}\right|_{\eta_r=0} = \frac{-\mathrm{j}\tilde{\mathbf{W}}^{\mathrm{H}}\mathbf{K}_r\tilde{\mathbf{W}}}{\tilde{\mathbf{W}}^{\mathrm{H}}\mathbf{K}'\tilde{\mathbf{W}}}, \quad \left.\frac{\partial\kappa_d}{\partial\eta_p}\right|_{\eta_p=0} = \frac{-\mathrm{j}\tilde{\mathbf{W}}^{\mathrm{H}}\mathbf{K}_p\tilde{\mathbf{W}}}{\tilde{\mathbf{W}}^{\mathrm{H}}\mathbf{K}'\tilde{\mathbf{W}}}, \tag{15}$$

where $\mathbf{K} = \mathbf{K}_r + \mathbf{K}_p$. Therefore, the damped wavenumber is obtained as

$$\kappa_d = \kappa - \mathrm{j}\frac{\tilde{\mathbf{W}}^{\mathrm{H}}(\mathbf{K}_r\eta_r + \mathbf{K}_p\eta_p)\tilde{\mathbf{W}}}{\tilde{\mathbf{W}}^{\mathrm{H}}\mathbf{K}'\tilde{\mathbf{W}}}. \tag{16}$$

Finally the decay rates of waves propagating along the track can be evaluated from the imaginary part of κ_d as

$$\Delta = 8.686\frac{\tilde{\mathbf{W}}^{\mathrm{H}}(\mathbf{K}_r\eta_r + \mathbf{K}_p\eta_p)\tilde{\mathbf{W}}}{\tilde{\mathbf{W}}^{\mathrm{H}}\mathbf{K}'\tilde{\mathbf{W}}}. \tag{17}$$

As presented above, the damping loss factors of the rail and rail pad are required for this track model. In practice both may be frequency-dependent. In this section, however, the damping loss factors of the rail and rail pad are set to constant values of 0.0002 and 0.2, respectively. η_r was chosen to represent typical material damping loss factors of steel. As specified here, the damping of the rail pad corresponds to typical values [4,5] and is a thousand times higher than that of the rail.

The predicted decay rates are shown in Fig. 3. Fig. 3(a) illustrates predicted results for the vertical and symmetric longitudinal waves and Fig. 3(b) shows those for the lateral, torsional and antisymmetric longitudinal waves. At the cut-on frequencies of each wave, the decay rates become infinite because the group velocities are zero at those frequencies. Note that the dispersion curves created for a given boundary condition (i.e., symmetric or antisymmetric boundary conditions in the mid-plane) do not cross each other. Instead, the waves swap their deformation shapes when two dispersion curves come close [17]. Hence one has to be aware that when the deformation shapes are exchanged between two waves, their decay rates are also swapped. The simulated results in Fig. 3 indicate that the minimum decay rate is about 0.04 dB/m and seems to occur between 10 and 20 kHz.

In practice, a range of rail pads with different stiffnesses is used in track. This difference in stiffness will bring a change in $\mathbf{K}_p$ in Eq. (16) which will affect the imaginary part of the damped wavenumber. In order to investigate the effects of the foundation stiffness on decay rates, different values of stiffness are applied here.

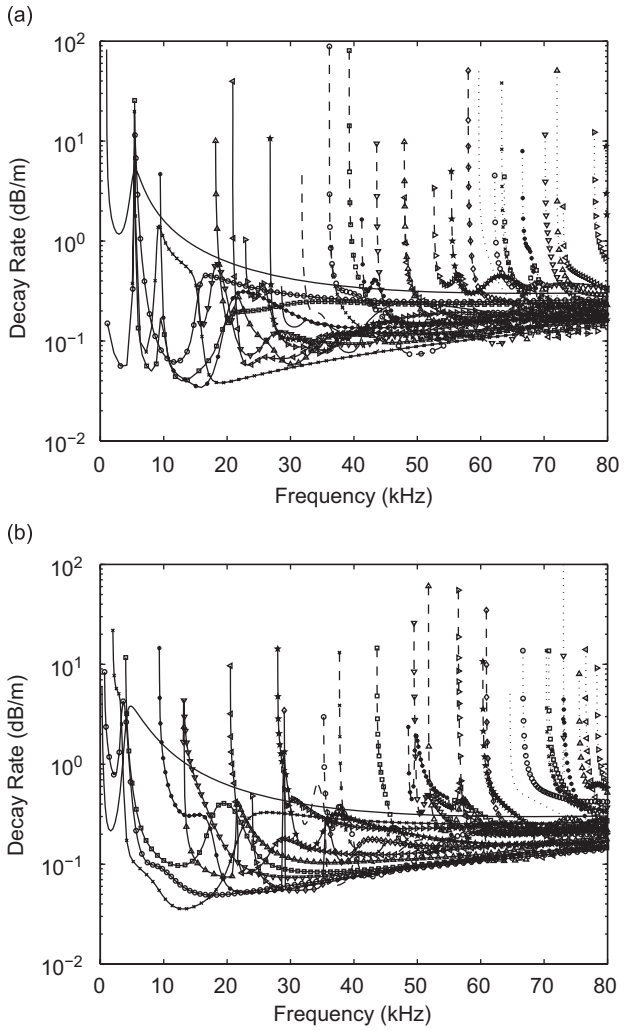

Fig. 3. Predicted decay rates of supported rail for (a) the vertical and symmetric longitudinal waves, (b) the lateral, torsional and antisymmetric longitudinal waves. The different line styles and markers correspond to Fig. 2.

The values chosen aim to represent the soft and stiff ends of the stiffness range of rail pads. In this prediction, the respective nominal stiffnesses of the soft and stiff rail pads are considered as 80 and 1500 MN/m in the vertical direction and 11 and 200 MN/m in the lateral direction, respectively [4,18]. (The chosen nominal stiffnesses of the rail pad for the decay rate calculation shown in Fig. 3 are 150 and 20 MN/m in the vertical and lateral directions, respectively.) In each case a factor of 10 is then applied to the stated nominal stiffnesses to represent the dynamic stiffening.

The predicted decay rates are presented in Figs. 4 and 5 for these soft and stiff foundation models. These figures show that with the soft pad there are more waves with low decay rates, whereas with the stiff pad most of the waves have higher decay rates. However, it turns out that the lowest decay rates for frequencies greater than around 20 kHz are not much different whether the rail pads are soft or stiff. This behaviour can be explained from the wave deformation shapes. Waves inducing large deformations in the rail pad are mainly affected by the stiffness changes in the foundation. In other words, the most slowly decaying waves propagate only through localized regions, such as the rail head and the web. Consequently, the decay rates of these localized waves are primarily dependent on the damping of the rail, not the rail pad. It is apparent from this sensitivity check that the lower limits of the decay rates at frequencies above 20 kHz are directly associated

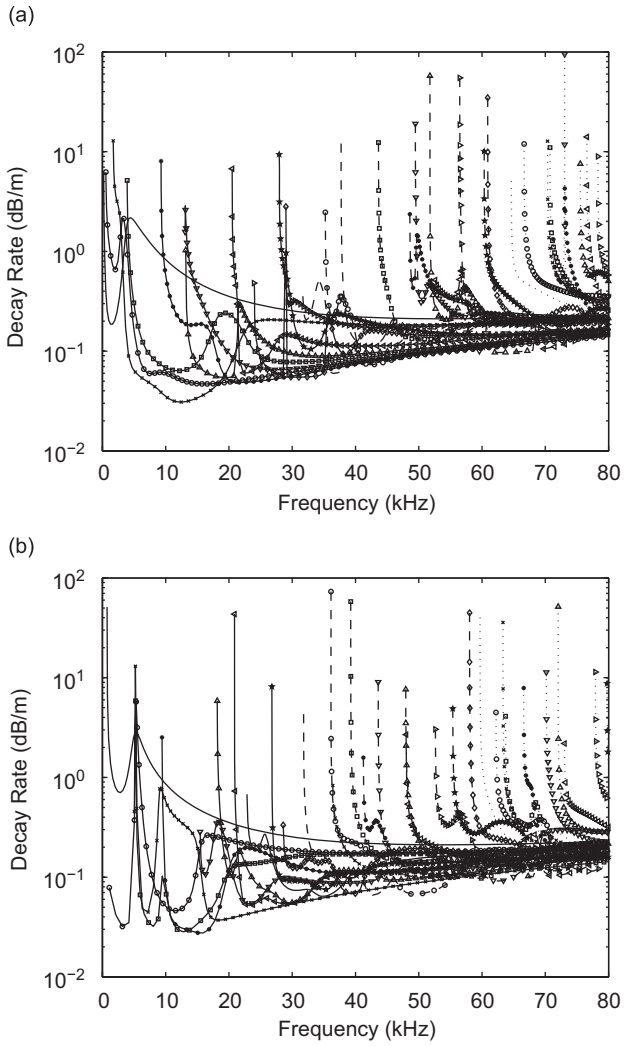

Fig. 4. Predicted decay rates of the rail on the soft rail pad for (a) the vertical and symmetric longitudinal waves, (b) the lateral, torsional and antisymmetric longitudinal waves. The line styles and markers correspond to Fig. 2.

only with the damping of the rail. Therefore, the damping of the rail is a principal factor in determining the long range wave propagation, even when the rail pad is quite stiff.

3.4. Improved decay rates using measured damping loss factor of a rail

In order to improve the simulated decay rates, damping loss factors are measured up to 80 kHz for three different samples of rail by means of impact hammer tests. Note that the damping loss factors measured in this experiment will include any acoustic damping caused by sound radiation from the surface of the rail samples, which is relatively small to the material damping of the rail.

For well separated modes of a structure, modal damping loss factor, η_n, of the nth resonance mode can be estimated from its resonance peak and half-power bandwidth using

$$\eta_n = \frac{\omega_b - \omega_a}{\omega_n}, \tag{18}$$

where ω_n is the resonance frequency of the nth mode, ω_a and ω_b denote its half-power frequencies, i.e., the frequencies at which the response is 3 dB lower than the resonance peak value [19].

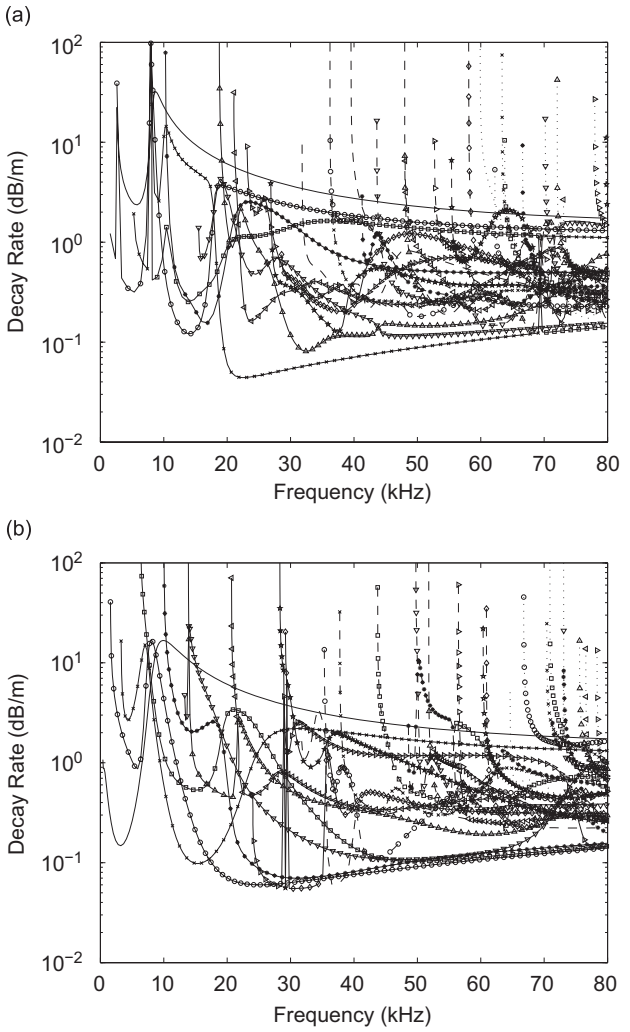

Fig. 5. Predicted decay rates of the rail on the stiff rail pad for (a) the vertical and symmetric longitudinal waves, (b) the lateral, torsional and antisymmetric longitudinal waves. The line styles and markers correspond to Fig. 2.

Measurements have been carried out on three short sections of rail with minor differences in rail section and material. The lengths of the samples used are 0.6, 0.45 and 0.31 m, respectively. The rail specimens were excited by a miniature impact hammer, PCB086D80, at the top and side of the rail head and the responses were measured by accelerometers, PCB352C22, at two points on the top and side of the rail head for each excitation. (One section was only measured up to 40 kHz.)

As an example, Fig. 6 shows the frequency spectra of the input force and output acceleration levels measured from one of the samples up to 80 kHz. As shown in Fig. 6(a), the impact hammer does not provide a uniform force over the whole frequency span. However, there is sufficient energy, even at high frequencies, to excite the resonances of the structure. Also, it is observed from the response spectrum in Fig. 6(b) that the sensor's mounting resonance appears to be located between around 60 and 70 kHz, causing relatively large responses despite a small input force. Since the extraction of damping does not require a calibrated frequency response, however, this does not adversely affect the measurement.

Damping loss factors were extracted from the resonance peaks and their half-power bandwidth for all relatively large amplitude resonance peaks. The measured damping loss factors for all three rail samples are illustrated in Fig. 7 together with the approximate ones created using a moving average. As shown in this figure, the extracted damping loss factors vary greatly from mode to mode at lower frequencies. Despite these

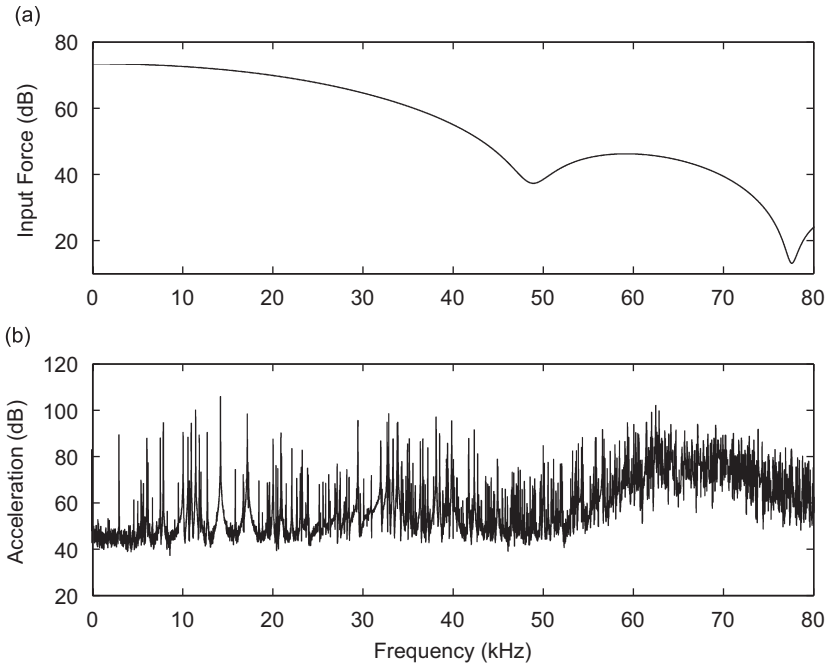

Fig. 6. An example of measured response. (a) Frequency spectrum of an input force, (b) averaged response spectrum of rail sample measured at the top of the rail head.

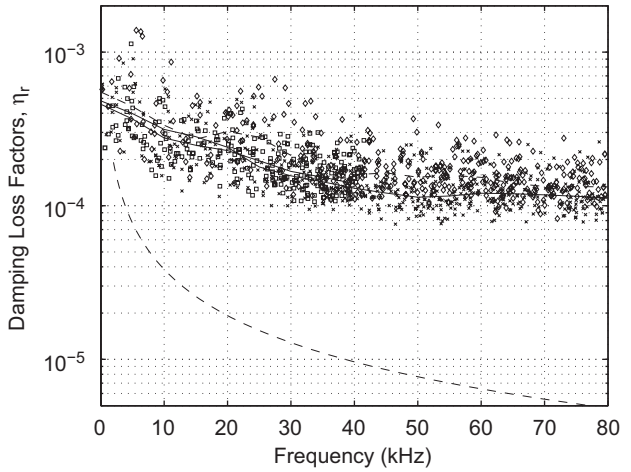

Fig. 7. Measured and moving averaged damping loss factors for the three different types of rail samples. ×, rail A; □, rail B; ◇, rail C; ——, approximated for rail A; —, approximated for rail B; — —, approximated for rail C; – –, due to acoustic emission predicted.

variations, the experimental results reveal that the damping loss factors of the rails tend to decrease quite rapidly until about 30 kHz and then more slowly at higher frequencies.

An estimate for the loss factor due to acoustic emission is also shown in Fig. 7. This loss factor was estimated from equations for the radiated power per unit length given by

$$P = \sigma\rho c S\overline{v^2} = m\overline{v^2}\omega\eta_a, \tag{19}$$

where η_a is damping loss factor due to acoustic emission, ρ is the density of air, c is the speed of sound in air, S is the perimeter length of the rail cross-section (projected in the direction of motion), $\overline{v^2}$ is the space averaged

mean square velocity and m is the mass per unit length of the rail. It is assumed that the radiation efficiency, σ, is unity at the high frequencies considered in the present paper, so the damping loss factor due to acoustic emission is given by

$$\eta_a = \frac{\rho c S}{m\omega}. \tag{20}$$

For the rail used here, $m = 60\,\mathrm{kg/m}$, $\rho c = 415\,\mathrm{kg/m^2\,s}$ and S will be about 0.35 m for vertical (or lateral) vibrations. For motion of, for example, only the rail head, both S and m will be reduced but η_a will not change much. From this it is clear that the loss factor due to acoustic emission is much smaller than the measured values, which can therefore be assumed to be dominated by material losses.

It was identified from this experiment that the three rail samples have very similar damping loss factors. In addition, it turned out from this experiment that the measured results did not differ greatly from the estimated damping loss factor of 0.0002, used for the initial decay rate prediction. For the rest of the work reported here, the moving average curve representing the approximate damping loss factor of rail sample A is used to improve the accuracy of the simulated decay rates.

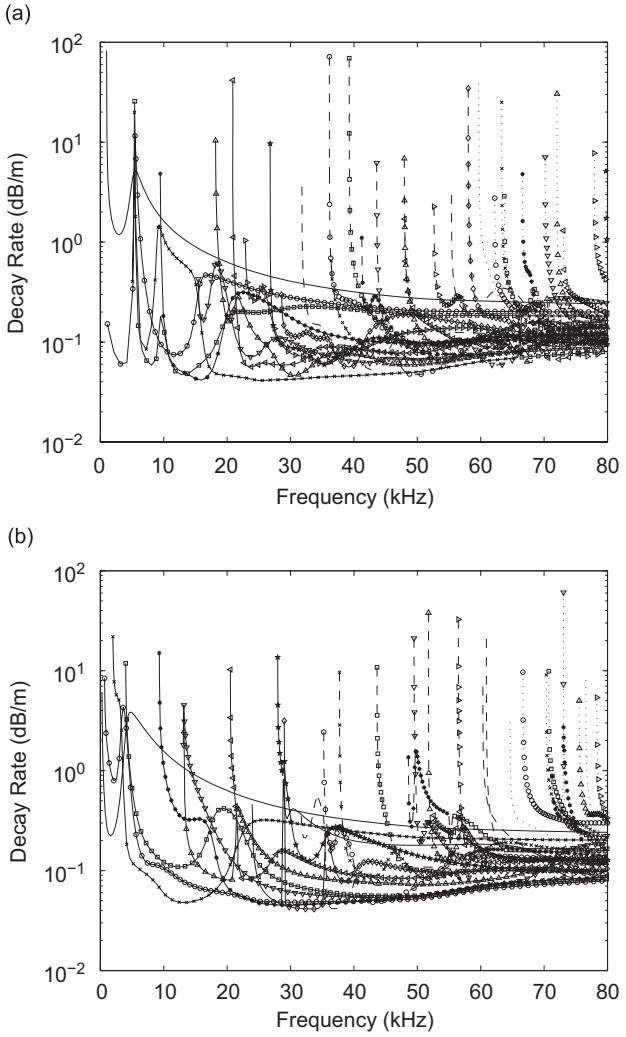

Fig. 8. Decay rates predicted by using the measured damping of rail A for (a) the vertical and symmetric longitudinal waves, (b) the lateral, torsional and antisymmetric longitudinal waves. The line styles and markers correspond to Fig. 2.

The revised decay rates are illustrated in Fig. 8 by using these measured damping loss factors. Comparing these results with the previous ones shown in Fig. 3, it can be seen that using the measured damping loss factor of the rail causes the curves with low decay rates to increase at frequencies below 25 kHz and to reduce above 25 kHz. Particularly, the lowest decay rate curves were modified most because they are most strongly affected by the damping loss factor of the rail. From this decay rate recalculation, it was found that the minimum values of decay rate are little changed but the frequency range where the minimum decay rates occur becomes somewhat broader, moving to the range between 20 and 40 kHz.

3.5. Decay rates of waves measurable on the rail surface

As found in Fig. 2, there are 63 different waves propagating below 80 kHz in this track model. To identify waves that are measurable in particular regions of the rail surface, the 'energy' associated with different parts of the rail surface was calculated from the displacement predicted by the WFE method [3]. For this purpose, three separate regions were specified on the rail surface, as shown in Fig. 9. These are the top of the rail head, the side of the rail head and the middle of the web. In this figure, y and z denote lateral and vertical directions, respectively. Then a metric which represents the normalized energies for each region and each direction was calculated using

$$Q_{j,z} = \frac{\frac{1}{n_j}\sum_{n_j}|\tilde{\mathbf{W}}_{z,j}|^2}{\frac{1}{N}\sum_{N}\|\tilde{\mathbf{W}}_{s}\|^2}, \tag{21}$$

where $\tilde{\mathbf{W}}_s$ denotes displacements in all directions at nodes on the rail surface, $\| \ \|$ is the vector norm, $\tilde{\mathbf{W}}_{z,j}$ is displacement in the z direction (and similarly for the x and y directions) at nodes belonging to the region j, n_j is the number of nodes in the region j and N is the total number of nodes on the rail surface. Therefore, this quantity would depict implicitly which waves are measurable in region j among all the waves in the system.

The dispersion curves predicted at each region are illustrated in Fig. 10 in terms of the energy ratio given in Eq. (21). In this plot, a threshold was used to exclude waves which have a small energy ratio, in order to make the figures more comprehensible. Thus only the waves which satisfy the criterion, $Q_j/\max(Q_j) > 0.1$ in each figure, are included in Fig. 10. Also in order to distinguish between the less and more measurable waves, two degrees of darkness are used to plot the curves in Fig. 10. The less measurable waves which satisfy $0.1 < Q_j/\max(Q_j) \leqslant 0.2$ are plotted in grey, while the more measurable waves with $0.2 < Q_j/\max(Q_j)$ are plotted in black.

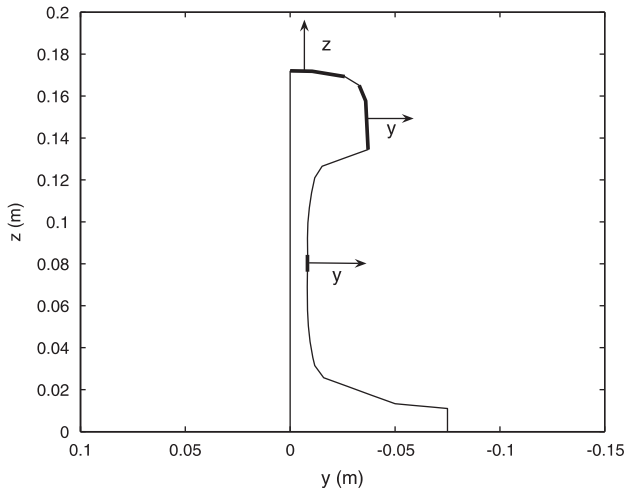

Fig. 9. Three regions and directions specified for the prediction of energy distribution on the rail surface.

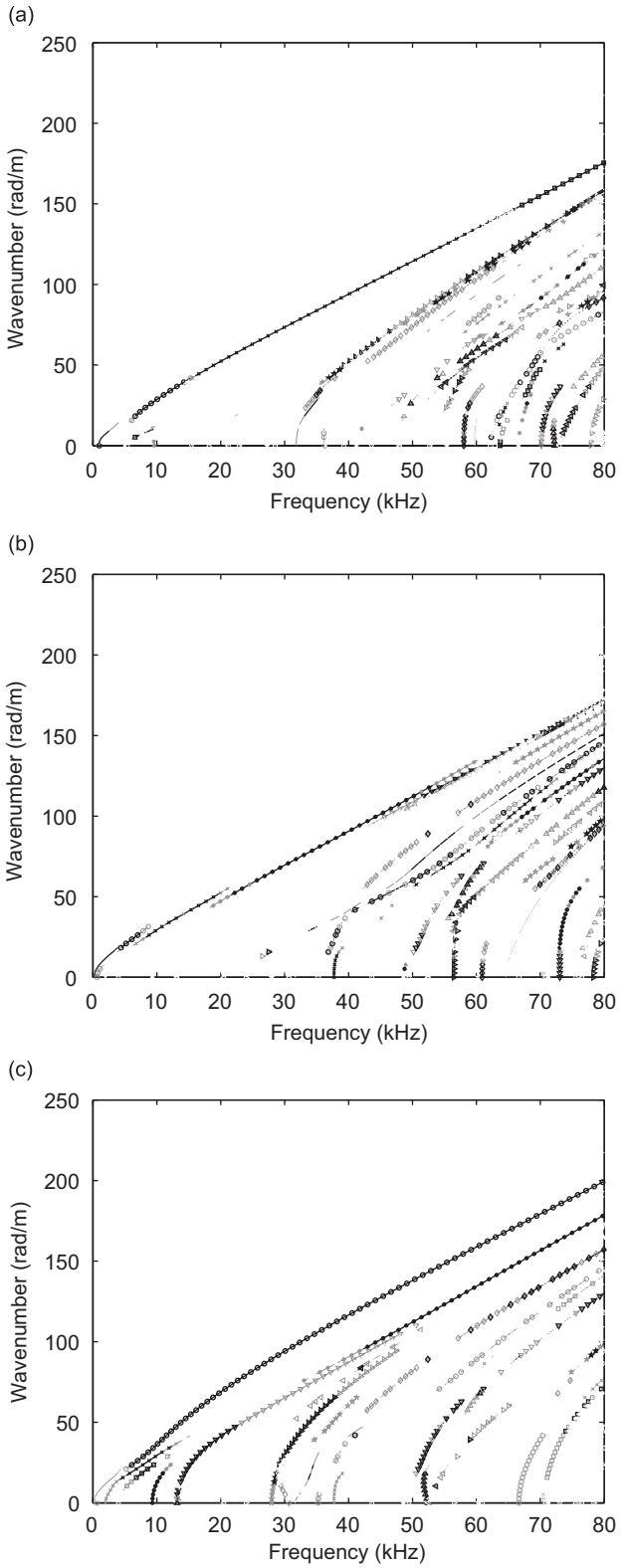

Fig. 10. Predicted dispersion curves with line intensity shown in terms of the energy for the vertical and lateral directions (a) at the top of the rail head, (b) at the side of the rail head, (c) at the middle of the web. The different line styles and markers correspond to Fig. 2.

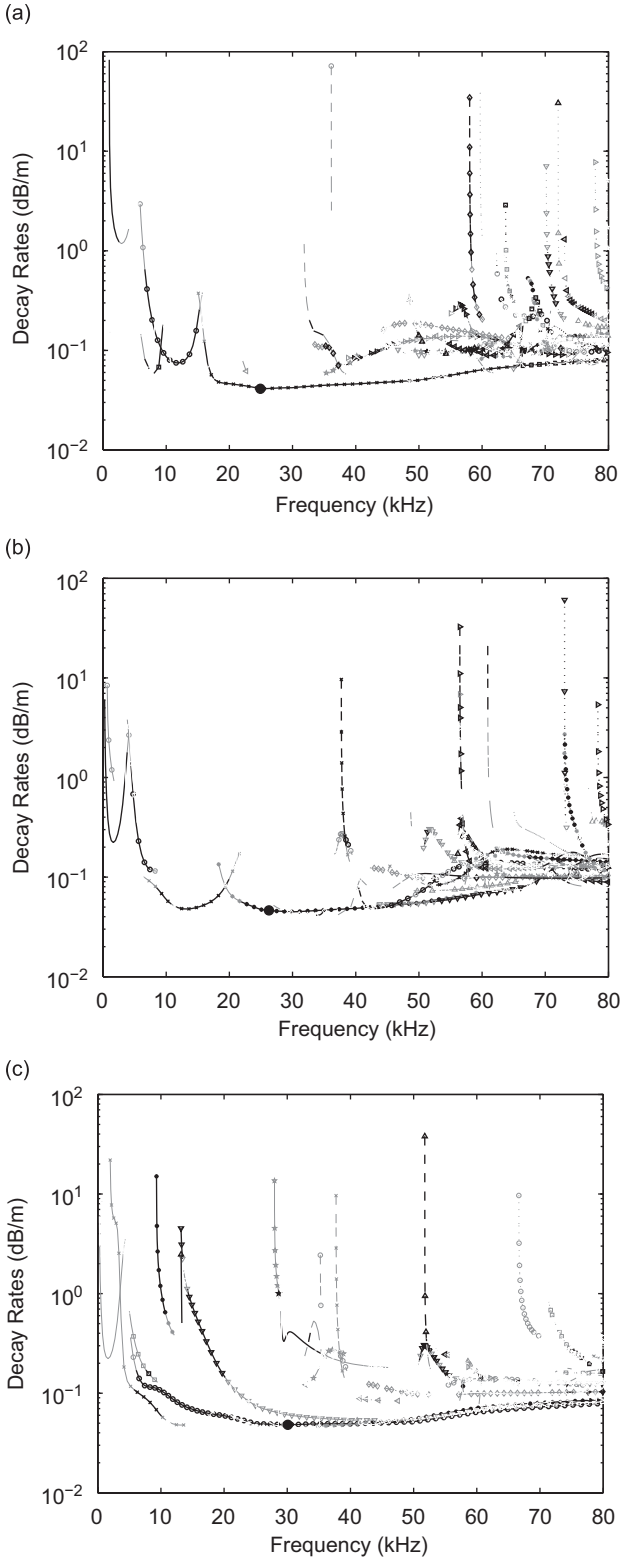

Fig. 11. Decay rates with line intensity shown in terms of the energy for the measurable waves predicted (a) at the top of the rail head in the vertical direction, (b) at the side of the rail head in the lateral direction, (c) at the middle of the web in the lateral direction. The line styles and markers correspond to Fig. 2.

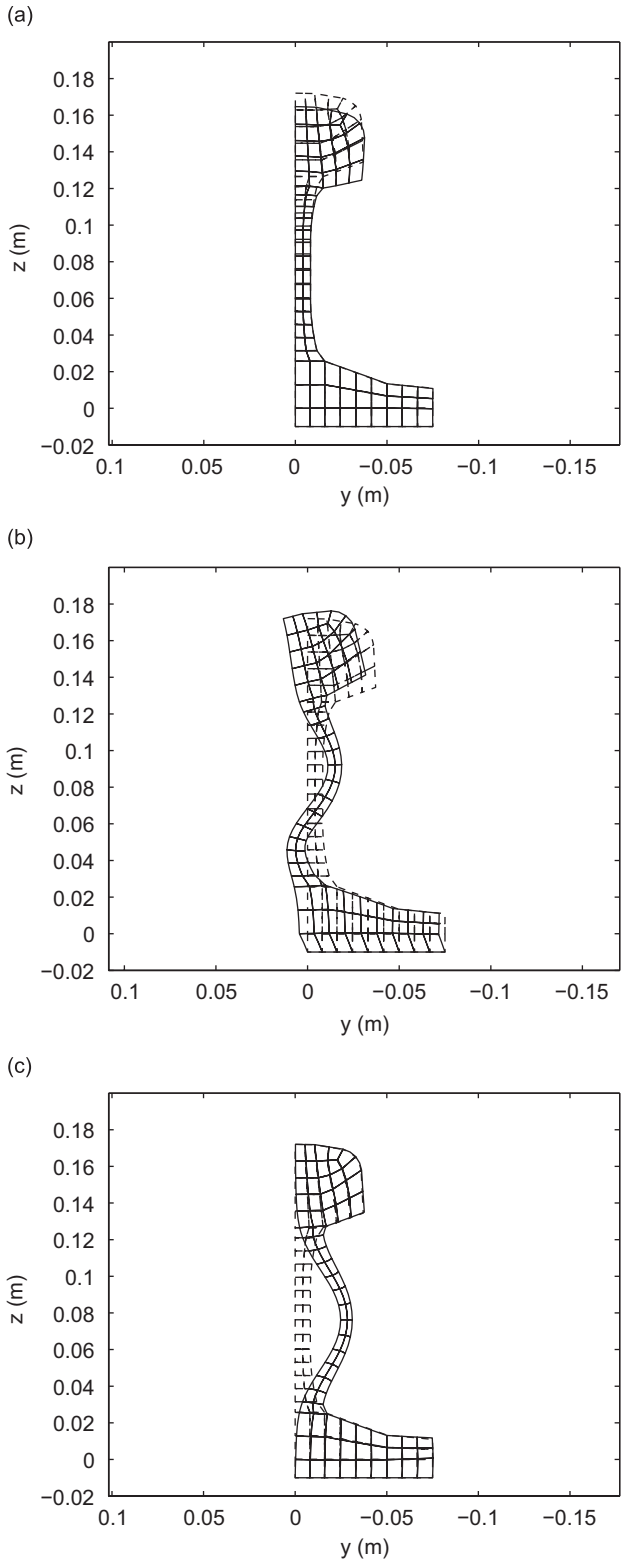

Fig. 12. The simulated deformation shapes of the waves (a) marked '•' in Fig. 11(a), (b) marked '•' in Fig. 11(b), (c) marked '•' in Fig. 11(c).

From Fig. 10(a), it can be seen that only a single type of wave is dominantly measurable at the top of the rail head below 32 kHz. A similar phenomenon is obtained at the side of the rail head for the lateral direction (Fig. 10(b)). At the middle of the web several waves are measurable throughout the frequency range (Fig. 10(c)). The most measurable waves at each region were identified in Ref. [3]. They are a vertical bending wave in the rail head, a lateral bending wave which has global deformation including the web and rail head and the first-order web bending wave, respectively.

The decay rates of the waves that are measurable at the top/side of the rail head and at the middle of the web are shown in Fig. 11. It is found from Fig. 11 that the minimum decay rates measurable on the rail surface tend to be about 0.04 dB/m at the top and side of the rail head and about 0.05 dB/m at the middle of the web, respectively. The wave types that possess the minimum decay rates are marked '•' in Fig. 11 and their deformation shapes are illustrated in Fig. 12. This figure confirms that these waves are the vertical bending wave localized in the rail head, the lateral bending wave of the rail head with a global deformation of the web and the first-order web bending wave, as presented in Ref. [3]. The simulated decay rates in Fig. 11 will be compared with the field test results in the following section.

4. Validation with field measurement

In order to validate the simulated decay rates, it is necessary to carry out a measurement over a longer section of rail. This requires the use of an operational track. In this section, rail vibrations measured on an operational railway track are presented. These experiments were carried out with assistance from Balfour Beatty and Network Rail. Measurements were made for several running trains. The decay rates are extracted from the measured signals and then compared with the previous results simulated by WFE analysis.

4.1. Measurement setup

The field measurement was performed on the Up Slow track of the British West Coast Main Line in August 2006. This track was selected to satisfy the following requirements for the measurement: a continuously welded rail and at least 500 m of plain line before and after the test site with no expansion joints, insulated rail joints or switches and crossings. This track has concrete sleepers but detailed information on the track components, such as rail geometry, support type, welds, etc., is not available. In the case of welds, in general, rails have flash-butt welds at 18 m distances and aluminothermic welds every 100 or 200 m. The former ones are expected to reflect little energy so they can be neglected. The aluminothermic ones introduce a certain amount of energy reflection but it is limited to the waves propagating through the web [3] and its reduction level would not be significant [15], limited to an increment in the decay rate of less than 0.01 dB/m.

Three miniature accelerometers, PCB 352C22, were used to detect the waves at different points on the rail cross-section: the field side of the rail head, the underside of the rail head and the middle of the rail web as shown in Fig. 13. The underside of the rail head was shown in numerical simulations to give very similar responses to the top of the rail head and this was validated from a separate measurement on a test track [15].

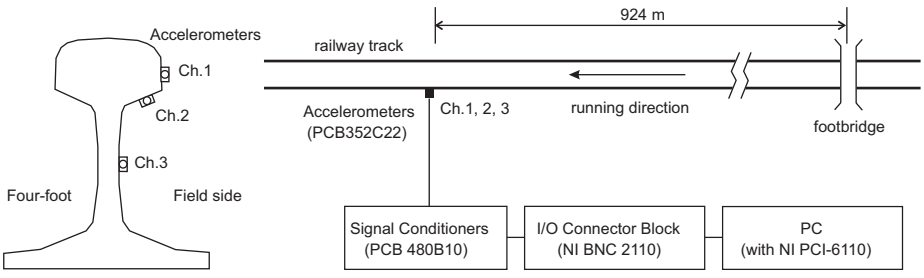

Fig. 13. Experimental setup for the field measurement.

Table 2
Details of the service trains measured from the field test

File name	Train type	Speed (km/h)	
		Average	Instantaneous
Train 1	4-car Class 321	109	119
Train 2	4-car Class 321	111	116
Train 3	8-car Class 350	166	162
Train 4	4-car Class 321	111	119
Train 5	4-car Class 321	123	132
Train 6	4-car Class 321	115	124

All accelerometers were mounted at a position midway between sleepers using glue. To provide electrical isolation (both for traction return currents and any signalling issues) a non-conductive laminate material of thickness 0.4 mm was inserted between the accelerometer and the rail. Instrumentation was installed by qualified personnel during a night-time track possession and the cables were run to a place of safety so that the measurements could be taken without any need for direct access to the operational railway. The equipment setup for this experiment is shown in Fig. 13. During the measurement, an observer was located on a footbridge which is 924 m in advance of the test site and gave a radio signal to warn of approaching trains so that the recording instrumentation could be switched on.

Rail vibration was recorded for six service trains, details of which are listed in Table 2. Most of them were of the same type and all were electric multiple units (EMUs) of either four or eight coaches. For each train, time signals of 2 min duration were captured at a sampling rate of 200 kHz. The sampling rate was sufficient to capture data for analysis up to 80 kHz whilst avoiding excessively the large data files that would have been necessary for higher sampling rates. A suitable anti-aliasing filter was used. The train speeds listed in Table 2 were evaluated by two different methods. The average speeds in Table 2 were calculated from the elapsed time between passing the footbridge shown in Fig. 13 and passing the site. On the other hand, the instantaneous speeds were found by using carriage lengths of each train and the elapsed time for a single carriage passage. The elapsed time for a single carriage passage was identified by means of the autocorrelation of the vibration measured at the middle of the web. It can be seen from Table 2 that the instantaneous speeds are slightly higher than the averaged ones in general. Based on these results, it is likely that trains were accelerating slightly when approaching the test site. However, since the speed profiles of the individual trains were not measured, the train's running distances have been estimated by using the instantaneous train speeds in the decay rate calculation.

4.2. Train-induced rail vibration

As an example of the measured time signals, captured time histories for train 1 are shown in Fig. 14 for the three measurement positions. These signals indicate that the train is passing the test site at between 42 and 45 s, inducing large rail vibrations at that time. According to these measured time signals, the response at the underside of the rail head is larger than the others, whereas the signal obtained from the middle of the web has the lowest amplitude.

The responses acquired while a train is passing the measurement point have been investigated in order to clarify the frequency characteristics of excitation which is generated by the wheel/rail rolling contact. The frequency spectra of the rail acceleration during the passage of the first bogie of train 1 are shown in Fig. 15. These were produced from the time signals between 42.7 and 42.9 s in Fig. 14. The frequency spectra in Fig. 15 show that each part of the rail cross-section is excited in a different manner. It is seen from this figure that the train induces a considerable rail vibration below about 3 kHz. This low frequency vibration of the rail is well explained by the wheel/rail rolling contact and is limited in frequency by the contact filtering effect [20]. What is more interesting in the present context is that running trains are found to be capable of exciting the rails quite well even at much higher frequencies between 20 and 50 kHz. Another important outcome observed

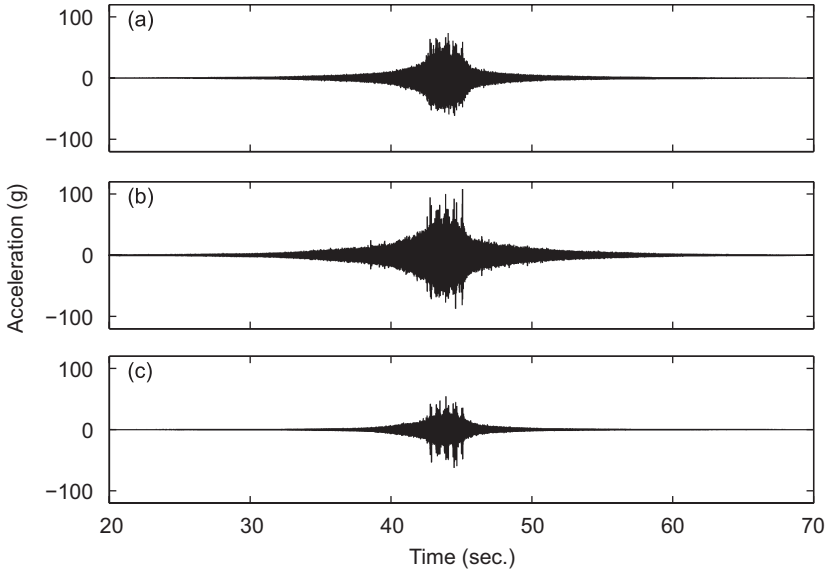

Fig. 14. Time signals for train 1 measured (a) at the side of the rail head, (b) at the underside of the rail head, (c) at the middle of the web.

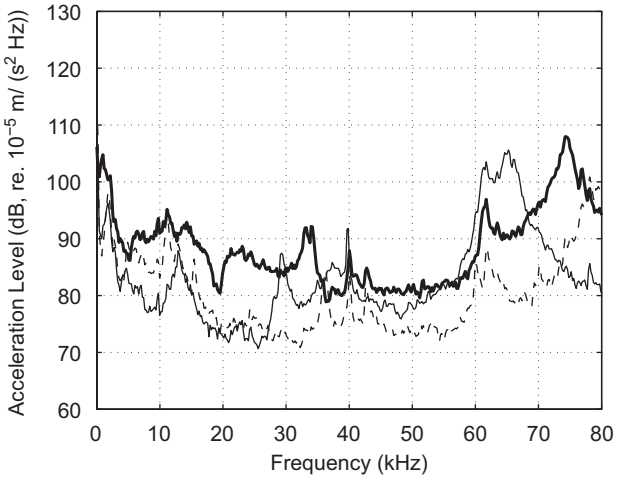

Fig. 15. Acceleration levels created by train 1 due to the wheel/rail rolling contact. —, at the side of the rail head; ▬, at the underside of the rail head; – –, at the middle of the web.

from this field measurement is that the rail vibrations measured from several trains have almost the same frequency characteristics despite being of two different types and with some variation in running speeds. The mechanism for this high frequency excitation was not identified yet. It should be noted that the large responses around 60 and 80 kHz for each channel resulted not from the physical responses of the rail itself but from the sensor's mounting resonances.

4.3. Measured decay rates

While a train is approaching or receding, the acceleration levels of the rail at a given frequency will increase or reduce with time. Decay rates can be obtained from the level difference between two train positions by dividing it by the train's running distance between them. As an example, spectrograms created for 0−90 s at

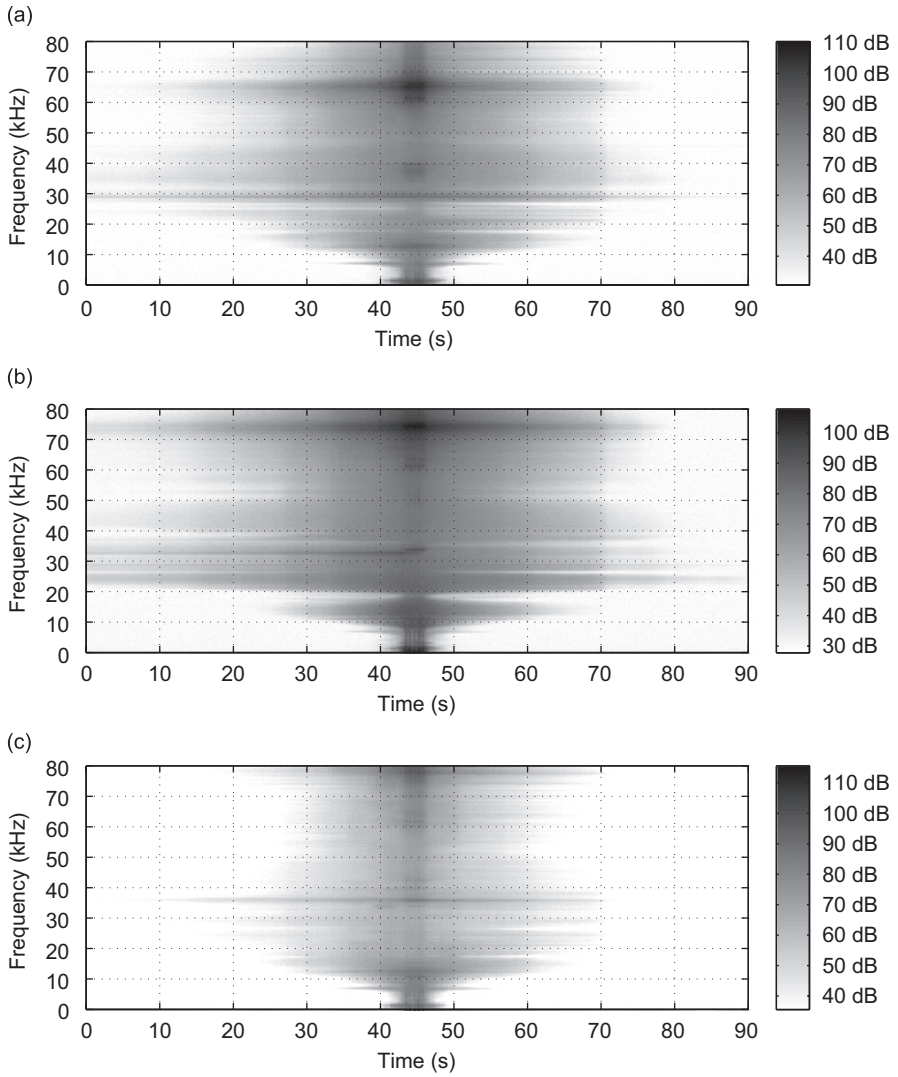

Fig. 16. Spectrograms for train 2 obtained (a) at the side of the rail head, (b) at the underside of the rail head, (c) at the middle of the web.

each measurement position are presented in Fig. 16 for train 2. From these spectrograms it is clearly visualized that the waves below 20 kHz decay very rapidly, particularly at the underside of the rail head. Conversely, at the underside of the rail head, some energy between 20 and 40 kHz is still measurable even about 40 s in advance of the train arrival.

For each train, decay rates were extracted from the acceleration level differences at 5 s intervals. The averaged decay rates obtained from the signals for all trains measured are shown in Fig. 17, together with the previous simulated ones. The measured decay rates below 10 kHz were disregarded in this comparison because the waves decay too rapidly in this frequency band, leaving just the background noise. It is found from Fig. 17 that the field test results agree very well with the simulated ones for all frequencies above 20 kHz. The comparison at the underside of the rail head in Fig. 17(b) suggests that the measured decay rate between 10 and 20 kHz corresponds to the simulated one but is shifted to slightly higher frequencies. This slight difference between the measured and simulated results may be associated with the rail geometry or the stiffness of the rail pad. The exact types of the rail and rail pads in the operational track or the extent to which the rail head is worn are not known. Nevertheless, the measured decay rates show considerable agreement with the predicted ones particularly between 20 and 50 kHz.

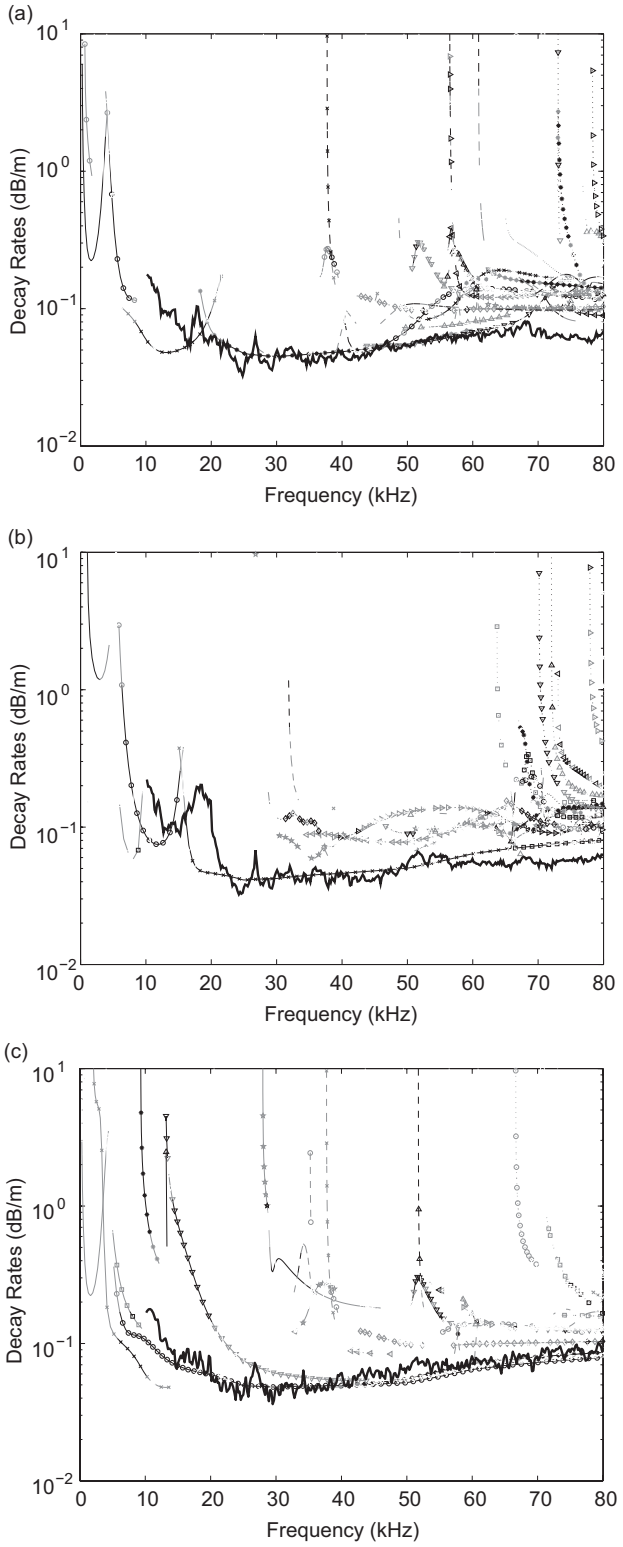

Fig. 17. Decay rates obtained from the field test, presented with the previous simulated results. (a) At the side of the rail head, (b) at the underside of the rail head, (c) at the middle of the web. ——, measured; the others, simulated. The line styles and markers in the simulated ones correspond to Fig. 2.

5. Conclusions

In this work, decay rates of waves propagating along a railway track were investigated in the frequency region up to 80 kHz by means of WFE analysis. From this prediction, it was identified that the decay rates of waves that propagate furthest are predominantly influenced by the damping of the rail, not by the damping of the rail pads. The damping loss factor of a rail was measured from several different rail samples as a function of frequency up to 80 kHz and found to be similar in each case. The simulated decay rates were modified using the measured damping of the rail.

In order to validate the simulated results, a field measurement was carried out on an operational railway track. Through this experiment, features of the train-induced rail vibration were obtained at the rail head and web. Also the minimum decay rates and frequency bands which are more likely to give the furthest detection range were identified from it. Consequently, it was validated from this field test that the measured decay rates coincide very well with the simulated ones across almost the entire frequency range up to 80 kHz.

Finally, the question of *how far along a rail can vibration travel*? could be answered clearly from the simulated and experimental results. The measured minimum decay rates and their corresponding frequency ranges are:

- about 0.04 dB/m at the underside of the rail head between 22 and 40 kHz;
- about 0.04 dB/m at the side of the rail head between 22 and 35 kHz;
- about 0.05 dB/m at the middle of the web between around 20 and 40 kHz.

These outcomes indicate that the most effective frequency range for long range wave propagation along railway tracks is between 20 and 40 kHz. This result might be different at other sites, with different rail conditions and with different trains.

It was seen from the field measurement that an amplitude range of more than 50 dB is measurable in the rail vibration. So, if a 50 dB level reduction is assumed, the maximum propagating distances that can be detected will be about 1.2 km at the rail head and about 1.0 km at the web, respectively. Also it was found from the field test that service trains are very effective in exciting rail vibration even at high frequencies. Furthermore, the characteristics of rail vibration induced by the different trains measured were almost the same, despite some differences in running speeds and train types. This may be because the trains measured were all EMUs, the two types being broadly similar. It also is likely that the roughness level of the rail surface is a very important parameter for rail vibration caused by wheel/rail rolling contact although its effect at these high frequencies has not been quantified. To assess more fully the effect of these parameters, further measurements would be necessary.

Acknowledgments

This work was supported by Balfour Beatty Rail Technologies. The authors are grateful to Barny Daley of Network Rail for making arrangements to enable access to the operational track for this research.

References

[1] J.L. Rose, M.J. Avioli, W.-J. Song, Application and potential of guided wave rail inspection, *Insight* 44 (2002) 353–358.
[2] J.L. Rose, M.J. Avioli, P. Mudge, R. Sanderson, Guided wave inspection potential of defects in rail, *Proceedings of Railway Engineering 2002*, *5th International Conference and Exhibition*, London, UK.
[3] J. Ryue, D.J. Thompson, P.R. White, D.R. Thompson, Investigation of propagating wave types in railway tracks at high frequencies, *Journal of Sound and Vibration* 315 (2008) 157–175.
[4] N. Vincent, D.J. Thompson, Track dynamic behaviour at high frequencies. Part 2: experimental results and comparisons with theory, *Vehicle System Dynamics Supplement* 24 (1995) 100–114.
[5] D.J. Thompson, N. Vincent, Track dynamic behaviour at high frequencies. Part 1: theoretical models and laboratory measurements, *Vehicle System Dynamics Supplement* 24 (1995) 86–99.
[6] D.J. Thompson, Experimental analysis of wave propagation in railway tracks, *Journal of Sound and Vibration* 203 (1997) 867–888.

[7] F. Lanza di Scalea, J. McNamara, Ultrasonic NDE of railroad tracks: air-coupled cross-sectional inspection and long-range inspection, *Insight* 45 (2003) 394–401.
[8] F. Lanza di Scalea, J. McNamara, Measuring high-frequency wave propagation in railroad tracks by joint time-frequency analysis, *Journal of Sound and Vibration* 273 (2004) 637–651.
[9] Research and Development Department, Long range screening of rail using guided waves, Third Vehicle/Track Interaction Course, Emmanuel College, Cambridge, UK, 2001.
[10] P. Wilcox, M. Evans, D. Alleyne, B. Pavlakovic, K. Vine, P. Cawley, M. Lowe, Long range inspection of rail using guided waves, *Proceedings of Railway Engineering 2002*, *5th International Conference and Exhibition*, London, UK, 2002.
[11] T. Hayashi, W.-J. Song, J.L. Rose, Guided wave dispersion curves for a bar with an arbitrary cross-section, a rod and rail example, *Ultrasonics* 41 (2003) 175–183.
[12] I. Bartoli, A. Marzani, F. Lanza di Scalea, E. Viola, Modeling wave propagation in damped waveguides of arbitrary cross-section, *Journal of Sound and Vibration* 295 (2006) 685–707.
[13] C.-M. Nilsson, Waveguide Finite Elements Applied on a Car Tyre, PhD Thesis, KTH, Stockholm, 2004.
[14] K. Knothe, S.L. Grassie, Modelling of railway track and vehicle/track interaction at high frequencies, *Vehicle System Dynamics* 22 (1993) 209–262.
[15] J. Ryue, Wave Propagation in Railway Tracks at High Frequencies. PhD Thesis, University of Southampton, UK, 2008.
[16] S. Finnveden, Evaluation of modal density and group velocity by a finite element method, *Journal of Sound and Vibration* 273 (2004) 51–75.
[17] N.C. Perkins, C.D. Mote, Jr., Comments on curve veering in eigenvalue problems, *Journal of Sound and Vibration* 106 (1986) 451–463.
[18] D.J. Thompson, J.W. Verheij, The dynamic behaviour of rail fasteners at high frequencies, *Applied Acoustics* 52 (1997) 1–17.
[19] D.J. Ewins, *Modal Testing: Theory and Practice*, Research Studies Press Ltd., Letchworth, 1984.
[20] P.J. Remington, Wheel/rail noise—part IV: rolling noise, *Journal of Sound and Vibration* 46 (1976) 419–436.